Journal of Power Sources 195 (2010) 2718–2730

Contents lists available at ScienceDirect

Journal of Power Sources

journal homepage: www.elsevier.com/locate/jpowsour

Gradation of mechanical properties in gas-diffusion electrode. Part 2: Heterogeneous carbon fiber and damage evolution in cell layers

K.K. Poornesh[a], C.D. Cho[a,*], G.B. Lee[b], Y.S. Tak[b]

[a] iASME Laboratory, Department of Mechanical Engineering, Inha University, 253 Yonghyun-Dong, Nam-Ku, 402-751 Incheon, South Korea
[b] Materials and Electro-Chemistry Laboratory, Department of Chemical Engineering, Inha University, Incheon, South Korea

ARTICLE INFO

Article history:
Received 10 October 2009
Received in revised form 6 November 2009
Accepted 6 November 2009
Available online 14 November 2009

Keywords:
Carbon fiber
Contact stiffness
Cohesive zone law
Damage propagation
Fracture toughness
Gas-diffusion electrode

ABSTRACT

In PEM fuel cell, gas-diffusion electrode (GDE) plays very significant role in force transmission from bipolar plate to the membrane. This paper investigates the effects of geometrical heterogeneities of gas-diffusion electrode layer (gas-diffusion layer (GDL) and catalyst layer (CL)) on mechanical damage evolution and propagation. We present a structural integrity principle of membrane electrode assembly (MEA) based on the interlayer stress transfer capacity and corresponding cell layer material response. Commonly observable damages such as rupture of hydrophobic coating and breakage of carbon fiber in gas-diffusion layer are attributed to the ductile to brittle phase transition within a single carbon fiber. Effect of material inhomogeneity on change in modulus, hardness, contact stiffness, and electrical contact resistance is also discussed. Fracture statistics of carbon fiber and variations in flexural strength of GDL are studied. The damage propagation in CL is perceived to be influenced by the type of gradation and the vicinity from which crack originates. Cohesive zone model has been proposed based on the traction–separation law to investigate the damage propagation throughout the two interfaces (carbon fiber/CL and CL/membrane).

1. Introduction

The commercial success of polymer electrolyte membrane (PEM) fuel cell depends on durability, stability, and reliability issues associated with the cell layers among which mechanical durability is still open for investigation on a much broader class. The power density of PEM fuel cell largely depends upon the coupled electro-chemical and electro-mechanical optimal functioning of the MEA. Many investigations and review articles have been reported recently on the electro-chemical and electro-mechanical durability of cell layers [1–10]. Durability is directly influenced by the degradation mechanism that is different for each layer (membrane, GDL, and CL). For example on a mechanical perspective, membrane, CL, and GDL differ due to their respective material responses of polymer, ductile, and brittle materials. Interplay among these failure modes is the key to understand the structural integrity principle especially near interfacial regions and the mechanical degradation of MEA.

There are number of reasons to study GDL on a mechanical perspective since gas diffusion with optimum flexural stiffness and high structural integrity remains to be the basic mechanical requirements for an ideal GDL [11,12]. One commonly referred problem with the GDL structural integrity is an uneven compression [13–17], which may possibly reduce the cell efficiency by directly affecting its porosity. Further, this will affect the water management ability of the whole cell and is considered as one of the major failure modes in fuel cell [4]. Compression of GDL also leads to carbon fiber breakage and deterioration of hydrophobic coatings as reported by Lin et al. [16] and Bazylak et al. [17]. Further, electrical contact resistance between GDL and bipolar plate (BPP) is considered as one of the major irreversible losses in PEM fuel cell. Researchers have developed various numerical models to predict the contact resistance and the recent advances relative to this field can be found elsewhere [18–24]. Very recently, Wu et al. [18] suggested two models—simplified model and generalized model. Simplified model considers only the elastic deformation near contact asperity, whereas, generalized model considers both the elastic deformation as well as carbon fiber bending. It can well be observed from their results that influence of the elastic deformation is dominative to the electrical resistance indicating the importance of material property responses in BPP as well as carbon fiber. On the other hand, GDL is primarily a carbon–carbon composite [25] where carbon fiber breakage (brittle material) and stress transfer from the broken fiber to intact fiber results in damage accumulation. Volume fraction of the matrix withholding carbon fibers is unknown and is assumed very less as compared to the fiber volume fraction. Further, GDL is a highly porous material (70% porosity) and thus carbon fibers play a key role in force transmission and energy absorption. Although there are experimental evidences suggesting

* Corresponding author. Tel.: +82 32 860 7321; fax: +82 32 868 1716.
E-mail address: cdcho@inha.ac.kr (C.D. Cho).

0378-7753/$ – see front matter © 2009 Elsevier B.V. All rights reserved.
doi:10.1016/j.jpowsour.2009.11.030

the structural failure of GDL, there are no attempts in developing precise numerical models to relate the failure of carbon fiber to GDL. This is because, GDL cannot be treated as a conventional composite material, and hence the classical design principles to define failure modes (e.g., shear failure; flexural strength) of composite material can no longer be applied here directly. In this article, we are presenting a single fiber damage model and flexural strength variation of GDL based on the fiber–bipolar plate (BPP) interaction.

Further, under the BPP land area, carbon fibers of GDL are subjected to compressive loading and under the channel area they are subjected to tensile loading. This nature of the loading followed by a partial unloading caused due to fuel cell operating conditions may cause carbon fiber fracture (tensile or compressive direction), provided the strength of the fiber exceeds its ultimate strength (fracture limit). Further, the 'heterogeneity' of GDL is very well established and it is worth noting that 'heterogeneity' of GDL in all literatures refer to random distribution of carbon fibers which are again compounded by the graded distribution of pores and binder material. However, studying at nano-level, our study predicts that the heterogeneity exists itself in the Teflon® coated carbon fibers which are the building units of GDL and are considered to be a supporting structure against the external compressive forces. As mentioned before, contact resistance is related to the elastic deformation in carbon fiber. Hence, it is highly possible that gradation in carbon fiber properties influences the variation in electrical contact resistance.

This article is broadly classified into two divisions. In the first part, flexural strength of GDL based on fracture toughness of carbon fiber and load transfer limit is investigated. In the second division, damage propagation in GDE is estimated with a special concentration on CL as well as GDL/CL and CL/membrane interfaces. GDL and CL are highly porous structures and hence are capable of absorbing higher amount of energy through a number of energy dissipation mechanisms (chemical or mechanical). It is learnt from our companion paper [26] that CL is a ductile material and it will follow a ductile damage over many loading cycles due to the plastic damage accumulation. Ductility enhancement is associated with the toughness increment in that it is actually related to evolution and motion of dislocations near the vicinity of critical damage. Habitually, ductile fracture is a strain controlled phenomenon unlike brittle fracture which is stress controlled.

Structural integrity principles near interfaces of MEA are explored in this study by evaluating the material response at nano-level. Damage evolution and delaminations are related to the stress transfer mechanism, which is again largely dependent of the cell layer inhomogeneity. Effect of hygrothermal and freeze/thaw cycling can only accelerate this delamination and material degradation. Therefore, justifying the fact that interfacial toughness and geometrical inhomogeneity plays a deciding factor in damage evolution and propagation in a cell layer, a cohesive zone model is developed to understand and investigate the effects of geometrical heterogeneities on the through-plane crack propagation.

2. Analytical models

2.1. Asperity size independent contact resistance model

At first, we define the electrical contact resistance between two conducting bodies as the ratio of change in voltage potential to the current passing through the constricted area. Hence we have

$$R_c = \frac{\Delta V}{I} = \frac{\rho_1 + \rho_2}{Q} \tag{1}$$

In Eq. (1), R_c is the contact resistance, ΔV is the voltage potential difference, I is electrical current. ρ_1, ρ_2, Q are electrical resistivity of carbon fiber, resistivity of BPP asperity and current flux density integrated over the constricted area, respectively. Evaluation of contact resistance between BPP and GDL requires the knowledge of carbon fiber bending and its elastic deformation by a BPP asperity. Elastic deformation is considered dominative and is used in overruling the contribution of fiber bending. Now, we assume that the relative motion at the asperity contact is governed only by the elastic deformation (δ_e); hence, by neglecting the inelastic deformation, relative motion (δ_r) near the contact asperity is equated to the elastic displacement as in the following equation:

$$\delta_r = \delta_e \tag{2}$$

Contact force (F_c) established by the surface asperity of BPP on carbon fiber can be related to fiber's stiffness (K) and the elastic deformation (force–displacement relation) and it is given as

$$F_c = K\delta_e \tag{3}$$

From the elastic-electrical analogy developed by Barber [27], we can have the following equation:

$$K = E_\gamma Q \tag{4}$$

where E_γ is the effective modulus and is expressed in terms of E_{bpp} (BPP modulus) and E_{cf} (carbon fiber modulus) and their Poisson's ratios—υ_1 and υ_2 as in the following equation:

$$E_\gamma = \left(\frac{E_{bpp}}{1-\upsilon_1^2} + \frac{E_{CF}(\delta_e)}{1-\upsilon_2^2} \right) \tag{5}$$

Contact stiffness can be related to Eq. (2) as follows:

$$K = K(\delta_e) \tag{6}$$

Now, electrical contact resistance can be reframed as follows:

$$R_c = \frac{(\rho_1 + \rho_2)E_\gamma}{K} \tag{7}$$

According to Eq. (5) and (6), contact stiffness and elastic modulus are increasing or decreasing function of elastic deformation in the fiber. Above is a simple analogy, which has significant information regarding the mechanical material property variation in single carbon fiber on electrical contact resistance variation. Present model is not restricted to spherical contacts that are commonly assumed in deriving the contact resistance near BPP/GDL interface.

Information regarding contact asperity size can be used in combination with the Eq. (7) to work this model as a contact asperity size dependent.

2.2. Failure model for single carbon fiber

Nanoindentation load–displacement data of single carbon fiber can be used for obtaining the stress–strain response of the fiber. Average stress (σ_c) on a single carbon fiber can be given as load (L) by indentation area (A_p):

$$\sigma_c = \frac{L}{A_p} \tag{8}$$

Strain (ε) estimation must consider the geometrical aspects of the indenter. In our experiment, Berkovich indenter is used and it has a very small radius (around 100 nm) at its tip. In case of spherical indenter, indenter strain is given by

$$\varepsilon \approx \frac{a}{R} \tag{9}$$

where R is the indenter radius and a is the radius of contact area at indentation (see Fig. 1(a)). It is noted from Eq. (9) and Fig. 1(a) that the above ratio is small and contact depth (h_c) is less than the maximum contact depth ($d_{\max}$).

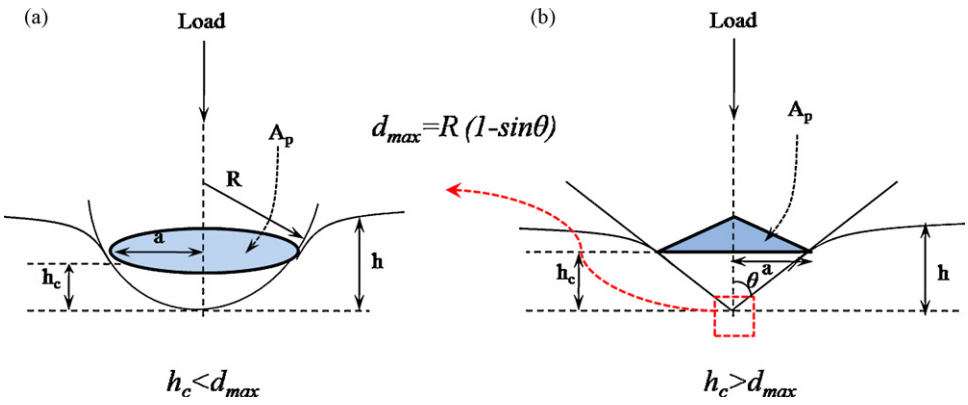

Fig. 1. Schematic of the indentation on a material surface (a) indenter with spherical tip (b) indenter with sharp conical tip.

For Berkovich indenter a/R ratio is very high and obviously $h_c > d_{\max}$ (Fig. 1(b)). Now the indentation strain is modified and given by the following equation [28]:

$$\varepsilon \approx \frac{\log(h_c)}{d_{\max}} + \frac{d_{\max}}{\sqrt{A_p(d_{\max})/\pi}} \tag{10}$$

Let us introduce a damage parameter (P_f) into stress–strain constitutive equation so that damage causes a softer elasticity as $E(1 - P_f)$. Then stress takes the form according to the following equation:

$$\sigma_c = E\varepsilon(1 - P_f) \tag{11}$$

From the weibull failure probability function, we can have the following equation:

$$P_f = 1 - e^{-(E\varepsilon/\sigma_0)^m} \tag{12}$$

Combining Eqs. (11) and (12) we can have the following equation:

$$\sigma = (E\varepsilon)e^{-(E\varepsilon/\sigma_0)^m} \tag{13}$$

The failure strain (ε_f) is obtained at $d\sigma/d\varepsilon = 0$. Then failure stress (σ_f)–strain (ε_f) can be calculated and related to weibull shape (m) and scale parameter (σ_0) as in the following equations:

$$\sigma_f = E\varepsilon_f e^{-1/m} \tag{14}$$

and

$$\varepsilon_f = \left(\frac{\sigma_0}{E}\right) m^{-1/m} \tag{15}$$

2.3. Flexural strength of GDL

GDL can be considered as a composite made of randomly distributed carbon fibers. Effective modulus (E_{rm}) of the randomly distributed fiber composite is given by [29]:

$$E_{rm} = \frac{2}{\pi}\int_0^{\pi/2} E(\theta)\, d\theta \tag{16}$$

Eq. (16) is based on the orientation dependence of carbon fibers and the fibers are uniformly distributed over the range of angles (θ) from $-\pi/2$ to $+\pi/2$. Simplified form of Eq. (16) can be used in estimating the GDL [29,30] and here it is used in combination with the fiber volume fraction:

$$E_{rm} = (0.375E_L + 0.625E_T)V_f \tag{17}$$

where E_L and E_T are the longitudinal and transverse modulus of the fiber, respectively. V_f is the volume fraction of fibers. There is a wide confusion over the fact that maximum shear stress is the driving force for GDL failure. This however, depends upon the fiber length and its load transfer capability. Since the volume fraction of the matrix is considerably less as compared to fiber volume fraction, the load bearing capacity solely depends upon the randomly distributed fibers. Furthermore, fiber length in GDL may vary in range from 3 to 20 mm. Failure strength prediction of GDL is related to the load transfer length of the short and long fibers.

Case 1. Fiber length < load transfer length

Assume a situation where the length of fiber under the BPP channel area is less than the load transfer length. Under this case, maximum fiber stress is less than the average fiber strength and hence fiber will not fracture regardless of magnitude of applied stress. Now, the shear stress plays an important role in defining the failure of GDL composite. Here, interfacial and carbon matrix failure takes place and ultimate strength of GDL ($(\sigma_{GDL})_u$) is calculated as in the following equation [29]:

$$(\sigma_{GDL})_u = \left(\frac{\tau l}{d}\right) V_f + (\sigma_m)_u V_m \tag{18}$$

In Eq. (18), τ is the shear strength between fiber/matrix interactions. l, d are length and diameter of the fiber, respectively. $(\sigma_m)_u$, and V_m are ultimate strength and volume fraction of the matrix, respectively. The above case is unlikely to be applied in fuel cell GDL. Even if the matrix fails, integrity of GDL remains unaltered as the volume fraction of the matrix is very less and hence the stress transfer takes place through the fibers.

Case 2. Fiber length > load transfer length

Consider a long fiber such that its length is larger than the load transfer length (l_c). In this case, fiber can be stressed to its maximum and hence its magnitude will be greater than the average stress. Failure of the composite takes place when breakage of the fiber initiates under the condition that maximum stress in the fiber reaches to its ultimate strength ($(\sigma_f)_u$).

$$(\sigma_{GDL})_u = (\sigma_f)_u \left(1 - \frac{l_c}{2l}\right) V_f \quad \text{when,} \quad V_m \ll V_{\min} \text{ and } l_c < l \tag{19}$$

where $V_{\min}$ is the minimum volume fraction of matrix.

In the above equation, the matrix contribution is neglected. Load transfer length of the fiber can be referred to the length of the fiber directly in contact with the BPP land area. Second term in the right hand side of the Eq. (19) approaches to unity as fiber length increases over load transfer length. The practicality of above equation to GDL is very real and it symbolizes the fact that structural integrity of GDL is related to ultimate

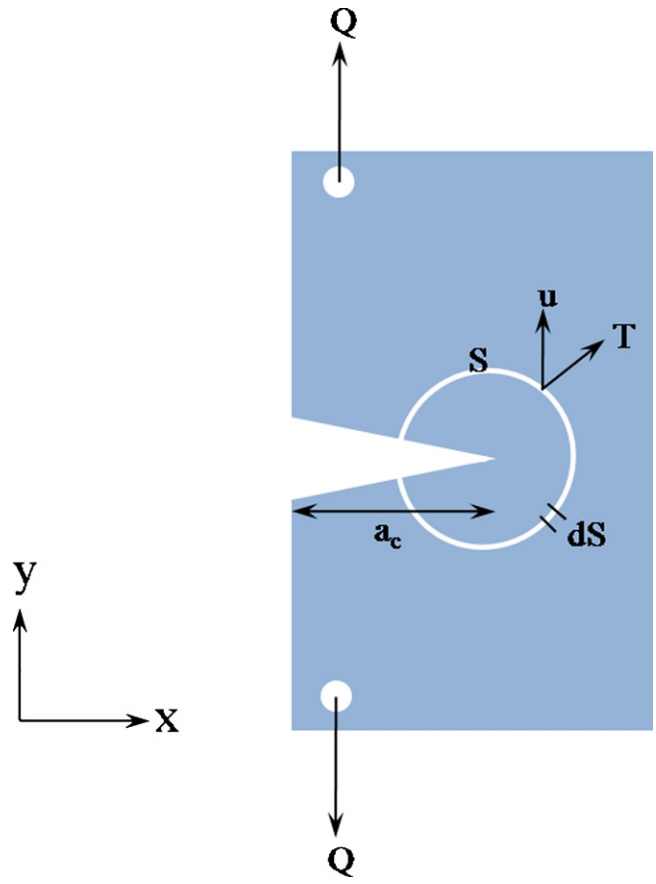

Fig. 2. Schematic of the pre-cracked elastic-plastic body subjected to tensile load *Q*.

strength of the fibers and not matrix. However, under the worst scenario of failure, long fibers may break down into small fibers and then Case 1 can be applied to incur a situation where a further failure of GDL depends upon the interconnecting matrix delaminations.

2.4. Crack propagation in CL

One can study the crack propagation in CL under different perspectives. CL can be perceived as an interlayer between the GDL and membrane. Load transfer characteristics from GDL to membrane depend upon the load bearing strength of the CL interlayer. Therefore, CL draws a considerable interest in studying the fracture related failures. The susceptibility of CL to undergo a fracture due in course with the mechanical load transfer becomes higher by hygrothermal cyclic loading, internal or surface defects, and geometrical heterogeneities. These will induce a local stress concentration at some critical locations which exceed the nominal strength (average stress per cross-sectional area) of CL, causing a fracture onset. Hence, even though the nominal stress is well below its fracture strength, local stress fields may ensure a local fracture. From this point onward, fracture propagation becomes important. Present study revolves around the prediction of the crack propagation or mitigation in a graded CL under the influence of yield stress gradient.

Consider a pre-cracked body subjected to load Q at the both the ends as shown in Fig. 2. Assume the elastic–plastic material behavior with the yield stress σ_y. Then the total potential energy (P_m) in the body is the sum of stored potential energy (P_e) and the potential energy of the applied loading (P_q) and is given by the following equations:

$$P_m = P_e + P_q \tag{20}$$

also

$$P_m = \int_A \omega \, dA - \int_S \mathbf{T} \cdot u \, dS \tag{21}$$

where S is the contour enclosing the crack tip, ds is the element of arc on this curve, $\mathbf{T}$ is the traction vector acting along the curve and u is the displacement vector (Fig. 2). In Eq. (21), ω is the strain energy density per unit volume and is given by the following equation:

$$\omega = \omega(x, y) = \omega(\varepsilon) = \int_0^{\varepsilon} \sigma d\varepsilon \tag{22}$$

Now differentiating Eq. (21) with respect to crack length, a_c, we derive an expression for J-integral as

$$-\frac{\partial P_m}{\partial a_c} = \int_S \left((\omega dy) - \mathbf{T} \cdot \left(\frac{\partial u}{\partial x} \right) dS \right) = J \tag{23}$$

Hence the decrease in the potential energy of a body in terms of its thickness, t, is given by the following equation:

$$J = -\frac{1}{t} \frac{\partial P_m}{\partial a_c} \tag{24}$$

Eq. (24) is the driving force for crack under constant modulus, yield strength, and geometry. It is generally referred as J-integral. Applicability of Eq. (24) is delimited when there are variations or gradations in the yield strength and modulus. As detailed by Kolednik [31], it is possible to attain a solution for crack driving force in terms of yield strength variation by holding other variables such as modulus and crack length as constant. This is, however, unlikely to be applied to a situation like CL where the consistent variation in modulus and the yield strength along the crack propagation direction is no longer assumed constant. Hence, let us consider a J-integral near the crack tip having a value of J_{tip} and far field J-integral (contour containing the entire plastic zone) having value of J_{ff}. Now, these two parameters can be related to each other to predict the gradient nature of the crack propagation. According to Sugimura et al. [32] and Kim and Suresh [33], the two J-integral are related as follows:

$$J_{tip} = J_{ff} F \left(\frac{K_I}{\sigma_y \sqrt{t}} \right) \tag{25}$$

Hence, depending upon the crack tip stress intensity we can decide on the crack propagation, which is again influenced by stress intensity (K_I) and material yield strength (σ_y).

2.5. Cohesive zone model

Recent experimental investigations have concluded that catalyst layer degradation is characterized by a cracking or delamination of the layer, catalyst ripening, catalyst particle migration, electrolyte dissolution, and agglomeration of Pt particles [1–6]. Broadly, these degradation behaviors are linked to chemical and thermo-mechanical operation of fuel cell. In an effort to understand the effect of heterogeneity of CL on its mechanical strength, we have experimentally studied the mechanical property variations along its thickness, mainly caused due to Pt/C particle gradations, as reported in our companion paper [26]. It is suggested that the local stress concentration in CL near interfacial zone lead to damage accumulation and hence damage evolution in CL from which cracks begins to show. In contrast to our belief, Rong et al. [34,35] proposed a mechanical model based on cohesive zone law to reason the evolution of cracks and delaminations induced by hygrothermal cyclic strain in a particle/matrix based approach.

Parameters involved in formulating the cohesive law (discussed in Section 3) are much of a scale dependent, i.e., they are not constant in each of continuum ('mm' scale), particle ('μm' scale), and atomistic ('nm') scale. Hence, application of cohesive law for a particle/matrix model of CL generally takes the atomistic form that involves a complex van der Waals interaction to be assigned to calculate the cohesive parameters [36,37].

Generally, a small pre-cracked zone is embedded in a body or interface and then LEFM (linear elastic fracture mechanics) concept is applied in obtaining the stress intensities and associated energy release rate to predict the crack propagation. Cohesive zone modeling is useful in modeling the larger fracture process zone where all the fracture processes occurring in a body are assumed to fall into cohesive line. In one such approach, traction–separation method uses the normal (or shear) traction and opening displacement (or sliding) as the criterion for debonding. Either the parameters (traction and displacement) are experimentally determined or they are assumed based on the relation between them. In the present study, the latter is chosen as the experimental determination involves a complex procedure and it must be near precision under micro-scale. Hence, most of the cohesive laws are phenomenological and thus a molecular dynamics simulation ('numerical' experiment) is required to approach the cohesive nature of the bonding.

Fig. 3(a) is the schematic representation of the three materials (carbon fiber, CL, and membrane) and their interfaces from where the model has been derived. Fig. 3(b) shows the numerical model for computing through-crack propagation in GDE. Crack tip is placed near the GDL/CL interface at a distance $y = 0$. Carbon fiber is modeled as a heterogeneous elastic material. For CL, three possibilities of property variations are considered since our major focus is to acquire the basic information regarding damage propagation in CL. Three cases are: increasing gradation (from GDL side), decreasing gradation (from GDL side), and homogeneous mechanical properties. A cohesive line (zone) is constructed ahead of the crack tip (at $y > 0$ and $y < 3.5$ μm) passing through two interfaces (GDL/CL and CL/membrane). Though cohesive zone represents physics of the fracture at the atomistic scale, it can be applied at the meso-scale by introducing energy dissipation mechanism. Hence, the cohesive zone is modeled as cohesive elements, which initially assume a linear elastic traction–separation behavior. Nominal tractions and nominal strains are related by element stiffnesses that depend upon the cohesive element thickness or length. Fig. 3(c) shows the cohesive element zone in CL. The opening separation is represented by a separation gap of 'δ'. The normal traction acts along the bridging elements and is denoted by $t(\delta)$, since its magnitude depends upon the interfacial separation δ. If it is perceived that traction represents a bonding interaction (or atomic interaction) between two bodies connected by a cohesive element, its value falls to zero beyond some critical separation, say $\delta_{n,f}$. Now, the process of damage can be easily understood by Fig. 3(d) and (e), and is explained as follows. In the present problem, for the decreasing case of gradation in CL, each of the cohesive elements in the cohesive zone is assigned with different traction–separation law such that maximum normal traction, $t_{n,\max}$, decreases in accordance with the assigned material properties. For increasing case of gradation in CL, the above approach is reversed. Fig. 3(d) shows a traction–separation law curves for some of the chosen elements from the cohesive zone. Fundamental concept of traction–separation curve is described in Fig. 3(e). As discussed before, the loading curve represents the elastic nature of the cohesive element with an initial stiffness value equal to E_c/T_c (E_c = modulus of cohesive element; T_c = cohesive element thickness). Then, the degradation of stiffness in the cohesive element begins to show up when normal traction reaches to its maximum value with respect to the assigned damage initiation criteria. The present study involves quadratic nominal stress criterion as a damage initiation and is given as in the following equation:

$$\sum_{i=n,s,t} \left(\frac{t_i}{t_{i,\max}} \right)^2 = 1 \tag{26}$$

where t is the traction vector and index i corresponds to normal, shear and second shear direction. According to the above criterion, damage is assumed to initiate when a quadratic interaction function either in a purely normal direction ($(t_n/t_{n,\max})^2$) to the interface or purely in the first ($(t_s/t_{s,\max})^2$) or second shear direction ($(t_t/t_{t,\max})^2$) reaches a value of one. In Fig. 3(e), red 'dot' depicts a damage onset point under pure normal traction direction from which damage begins to evolve. Hence, descending curve in Fig. 3(e) represents a damage evolution of cohesive element and it can be represented in terms of constitutive equation as given by the following equation:

$$[t_i]_{i=n,t,s} = [(1 - D)k][\delta_i]_{i=n,t,s} \tag{27}$$

In Eq. (27), D is the damage parameter and its value ranges from 0 to 1. From the point of damage initiation value of D evolves from 0 to 1. k represents initial stiffness of cohesive element. Area under the traction–separation curve is the energy dissipation (Γ) or the work of fracture as shown in Fig. 3(e). For the fictive crack tip (crack tip subjected to mixed mode loading) energy dissipation must be represented by mixed mode of failure. Fig. 3(f) explains the mixed mode traction–separation law where Mode I and Mode II represents a failure under normal and shear direction of traction, respectively. For the mixed mode damage evolution, fracture energy dissipation, Γ_c, is governed by well known B–K (Benzeggagh–Kenane) criterion [38] where critical fracture energy dissipation in both the shear directions (first and second) is equal ($\Gamma^s_{\mathrm{IIc}} = \Gamma^t_{\mathrm{IIc}}$) and is given by Eqs. (28) and (29):

$$\Gamma_{\mathrm{Ic}} + (\Gamma_{\mathrm{IIc}} - \Gamma_{\mathrm{Ic}}) \left(\frac{\Gamma_{shear}}{\Gamma_T} \right)^{\eta} = \Gamma_c \tag{28}$$

where Γ_{Ic} and Γ_{IIc} are the critical fracture energy dissipation in Mode I and Mode II, respectively. Total fracture energy is the summation of Mode I and Mode II fracture energies (Γ_{I} and Γ_{shear}) and is given according to the following equation:

$$\Gamma_T = \Gamma_{\mathrm{I}} + (\Gamma^s_{\mathrm{II}} + \Gamma^t_{\mathrm{II}}) = \Gamma_{\mathrm{I}} + \Gamma_{shear} \tag{29}$$

and η is the B–K parameter which maintains the shape of the failure point in the mixed mode plane shown in Fig. 3(f).

Under the mixed mode evolution of damage, effective displacement, δ_{eff}, should be mentioned and is given by the following equation:

$$\delta_{eff} = \sqrt{\delta_n^2 + \delta_s^2 + \delta_t^2} \tag{30}$$

All the elements are assigned a linear softening damage evolution.

It is always convenient to take energy based damage evolution of cohesive zone rather than approaching a strain based cohesive law. This can be justified by what follows. If we look at Eq. (25), stress intensity (K_{I}) is related to J-integral, i.e., energy release rate in the elastic-plastic fracture mechanics. Further, Eq. (22) refers to strain energy density and is related to stress–strain in a body. On the other hand, cohesive law is based on traction–separation law and is related to energy release rate or work of fracture (Fig. 3(e)). Hence, strain in traction–separation law (cohesive zone) becomes very unusual. This is the reason for not taking the hygrothermal strain based damage in cohesive elements in our model.

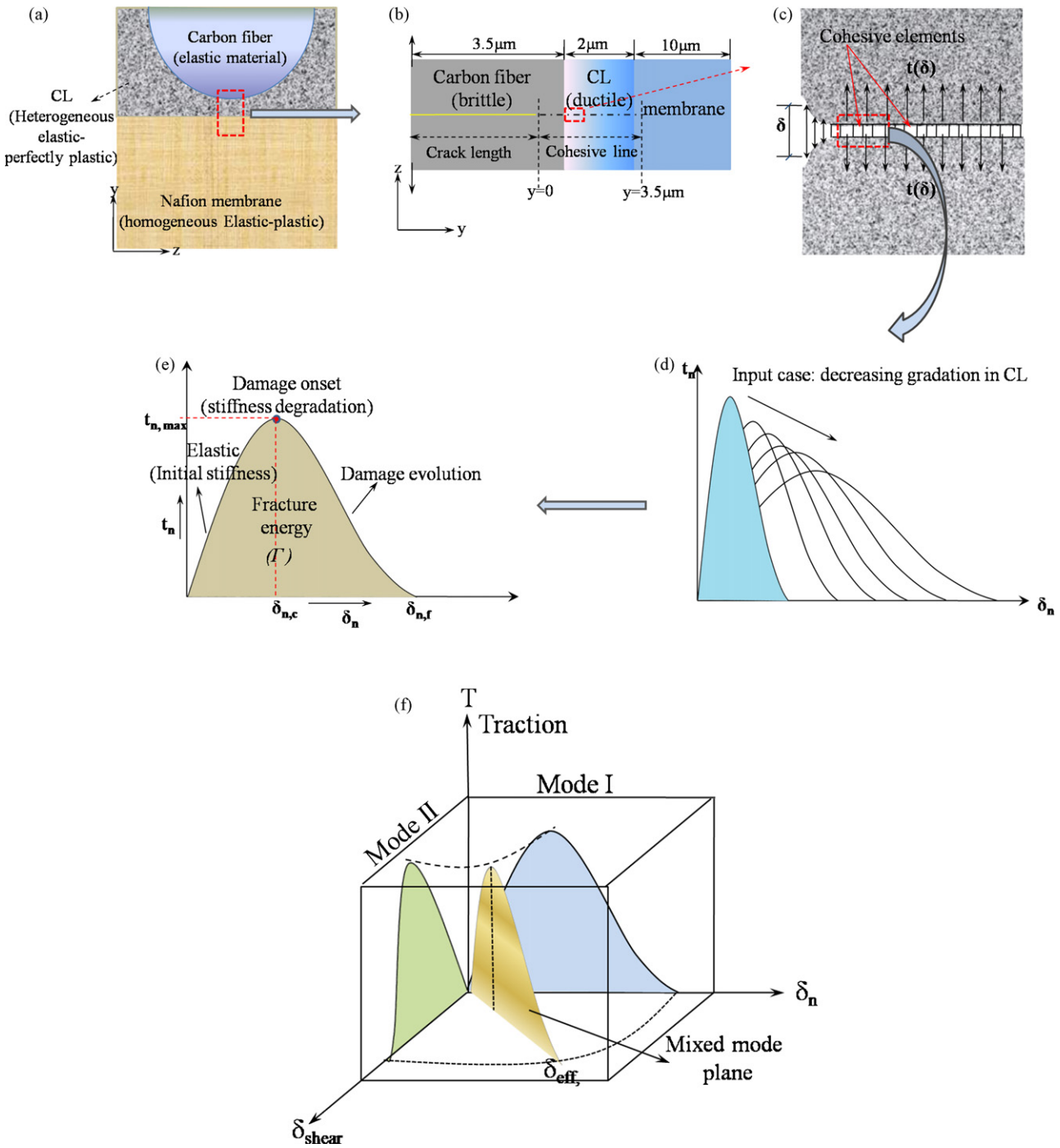

Fig. 3. Cohesive Zone model (a) interaction among three materials (carbon fiber, CL, and membrane) and corresponding interfaces. (b) Pre-cracked cohesive model with a crack tip placed near carbon fiber/CL interface. Dashed line ahead of crack tip indicates the cohesive line passing through two interfaces. (c) Magnified view of cohesive zone in CL showing the cohesive elements. (d) An example of the element-wise application of traction–separation law in a decreasing gradation case. (e) Fundamental concept of traction–separation law of one cohesive element. (f) Illustration of mixed mode response in a cohesive element.

3. Finite element analyses

3.1. Driving force for crack propagation in CL

Fig. 4 shows the FE model used for investigating the effect of geometrical heterogeneity on the crack propagation or mitigation principles. Single 'sandwich' model has been proposed instead of two separate models for each of the different gradation conditions of CL in order to closely monitor the differences. According to Fig. 4, an interlayer is inserted between two layers. Upper layer is modeled as CL with an increasing gradation whose mechanical properties vary according to the results obtained in Part 1. Lower layer is also modeled as CL but with a decreasing gradation in mechanical properties. For interlayer, two cases are studied. In first case, middle layer is assigned with the properties of carbon fiber and in second case it is modeled as the elastic-plastic material with the averaged properties of CL. Pre-existing through-plane crack with upper and lower crack tips are embedded in a middle layer. Both of the crack tips are close to the interfaces but are not connected with the adjacent layers. Purpose of choosing two material properties for middle

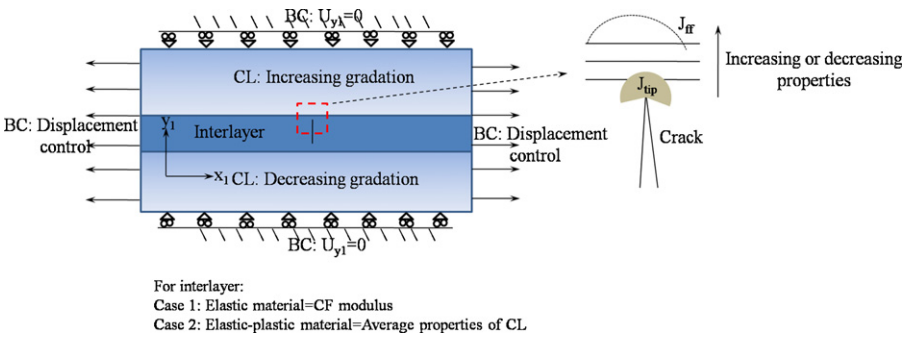

Fig. 4. Analysis model to predict the driving force for crack propagation. Figure shows three layers and corresponding boundary conditions. Crack is placed in interlayer at an equal distance behind the two interfaces. Enlarged view of crack tip describes the meaning of J_{tip} and J_{ff}.

layer is explained in Section 4. Fine finite element mesh is used around the crack tips. All layers are modeled with quadrilateral elements under plane stress condition. Top and bottom surfaces of the model are constrained in 'y_1' direction to zero. Side surfaces of the model are axially displacement controlled. The material behavior of CL is assumed to obey J2-flow (rate-independent) theory of plasticity. Constitutive equation for J2-flow theory or Ramberg–Osgood is given by the following equation:

$$\varepsilon = \frac{\sigma}{E_m} + \alpha\frac{\sigma_y}{E_m}\left(\frac{\sigma}{\sigma_y}\right)^{1/N} \tag{31}$$

where ε, σ, E_m, σ_y is tensile strain, tensile stress, elastic modulus and yield strength of the material, respectively. The term '$\alpha(\sigma_y/E_m)$' represents the yield offset in the stress–strain curve (in our study yield offset is assumed to be 0.002). And the material constant '$1/N$' is the strain hardening exponent. For elastic-perfectly plastic material value of N is zero and hence strain hardening takes an infinite value. However, value of 25, which is large enough to account for plasticity, is taken in our numerical analysis.

GDL is modeled as the elastic material (Case 1). Magnified view of crack tip is shown on the right side of Fig. 4 to understand the mechanics involved in the present investigation. J-integral ahead of the crack tip is calculated based on the energy release rate. In addition, far field J-integral represents an area encircling a complete plastic zone and hence monitoring this zone with respect to the crack tip integral gives an estimation about the crack propagation or mitigation. Straight lines represent the layers with the varying deformation plasticity values.

3.2. Cohesive zone model

Explanations regarding the cohesive zone model are already presented in Section 2. Cohesive zone model explained in Section 2.5 is generally applied in delamination related problems. However, its application can be extended to delamination related crack propagation where one can investigate the material property influence on the growing damage. Three cases are investigated here. In all the cases, mechanical properties of carbon fiber and membrane are maintained to remain same. Carbon fiber is modeled as a homogeneous elastic material with the modulus averaged on indentation result. Membrane is modeled as the elastic-plastic material whose properties are taken from [39]. Three cases are considered for CL: homogeneous, decreasing gradation, and increasing gradation (from GDL side). For homogeneous layer, averaged elastic-plastic properties are assigned according to the results obtained in our companion paper [26]. For the gradation properties, a smooth gradation is assigned element wise with the properties varying according to indentation results (increasing gradation) [26]. For the decreasing case of gradation, properties are precisely reversed. All three bodies are modeled with 4-node bilinear plane strain quadrilateral elements (CPE4R) available in the ABAQUS element library [38]. Cohesive element zone ahead of crack tip is modeled with 4-node 2-D cohesive elements (COH2D4). Refined mesh is preferred near the crack tip and is located near the GDL/CL interface. Total length of cohesive line is about 3 μm (2 μm in CL, 0.5 μm each in GDL and membrane). Interfacial lines are connected by a single cohesive element (in the cohesive zone) whose properties are averaged over the properties of adjacent cohesive elements.

Maximum traction in the normal and shear directions are two basic input parameters to represent damage initiation in a cohesive element. Second shear direction is assumed to be zero as the present problem is only 2-D. At the atomic scale, normal and shear traction takes the form equal to $E/10$ and $\sigma_y/1.732$, respectively (E is the elastic modulus of the material and σ_y is the yield strength) [34]. However, at the micro-scale these values are not reasonable because it is already mentioned that cohesive behavior is highly scale dependent. Hence, $E/10$ and $\sigma_y/1.732$ are divided again by 10^3 to approach the problem at micro-scale (This is the best possible assumption that we can have at this stage without any experimental evidence). Again, for elastic material (carbon fiber), parameters of cohesive elements are calculated based on modulus (gives the maximum traction in normal direction) and is made equal to the maximum traction in the shear direction. For CL, cohesive element properties vary according to the type of gradation (increase or decrease) introduced into it. This makes the problem highly complex, as the tendency towards solution convergence gets very narrow. Hence, it is highly recommended to use optimized cohesive elements based on its length and thickness, especially in case of gradation.

4. Results and discussions

4.1. Indentation results

Nanoindentation experiment on Teflon® coated carbon fiber is performed to evaluate the mechanical properties at nano-scale. Fig. 5 shows the indentation result of load and displacement response of a single carbon fiber. A slight elastic-plastic followed by an elastic response can be noted upon loading. Initial elastic-plastic response may have come from the Teflon® coating on carbon fiber. This significant transition from ductile to brittle phase explains the rupture and breakage of carbon fiber. Further, careful observation of loading curve reveals a single pop-in event and this behavior can be related to two major conclusions. In ductile material, 'pop-in' event generally refers to onset of yielding and in brittle material it refers to an internal local fracture. Hence, by judging the loading response as a linear function of displacement, carbon fiber is now classified as a brittle material with a fracture occurring at critical load. However, flexural strength (fracture toughness) of

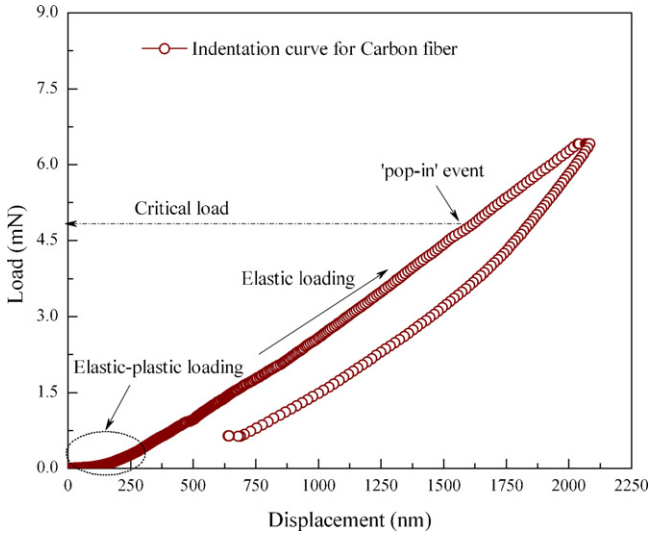

Fig. 5. Nanoindentation response of load vs. displacement for Teflon® coated carbon fiber. Transition from ductile phase to brittle phase can be observed. 'pop-in' event characterizes the local fracture in carbon fiber.

fiber may vary significantly at different locations. Hence, indentation responses at 20 different locations of carbon fiber are taken and the failure statistics of the fiber is plotted with the help of weibull probability distribution function and it is reported in Section 4.3.

Fig. 6 shows the hardness and modulus response as a function of indentation depth. Initial (<250 nm) decrease in the hardness and increase in the modulus may have resulted from the fiber coating. After the initial limit, hardness increases to some depth and then decreases gradually. Maximum value of transverse modulus for a carbon fiber in this case is found to be around 3.5 GPa and it decreases to 1 GPa as the indenter penetrates further to the core. If it is assumed that the carbon fiber has a diameter of 6–7 μm then indentation results presented here for 2 μm should be sufficient to explain the inhomogeneity of carbon fiber. The decreasing properties toward the fiber core are attributed to their texture and fabricated conditions.

In another remarkable finding, which finds its significance in contact related issues, contact stiffness data of carbon fiber is provided in Fig. 7 as a function of indentation depth. It can well be observed from Fig. 7 that contact stiffness increases linearly for a depth less than 250 nm, which is consistent with the results obtained for modulus and hardness. The slope of the contact stiffness decreases beyond 250 nm and maintains a value of 5000–6000 N m^{-1}.

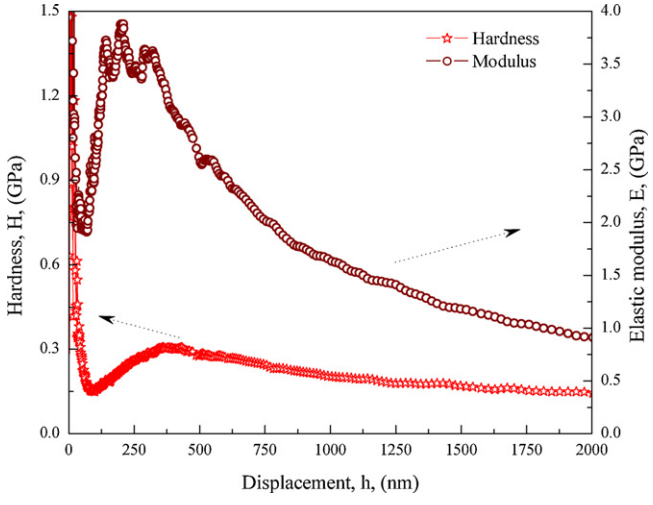

Fig. 6. Modulus and hardness response of carbon fiber with respect to the indentation displacement.

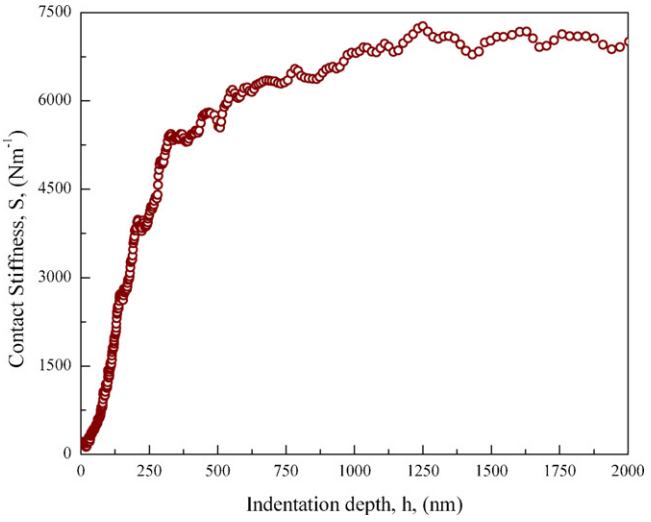

Fig. 7. Contact stiffness response over the indentation displacement of carbon fiber.

4.2. Influence on electrical contact resistance

Above obtained mechanical properties are applied to Eq. (7) in obtaining the contact resistance variation. Fig. 8 shows the calculated variation in electrical contact resistance as a function of elastic deformation in carbon fiber. Qualitative variation in contact resistance is given in ohms (Ω) and the quantification of the obtained result is represented in Ω-μm^2. Specific contact resistance is obtained by assuming a circular contact asperity on carbon fiber. BPP asperity radius is taken to be around 3.67 μm [18]. This application can be extended to any size or shape of the contact on carbon fiber. Exact definition of electrical contact resistance must involve bending contribution of fiber; however as explained before, its contribution is assumed less or insignificant. Further, contribution of Teflon® coating is not shown for the brevity, however it is found to give very high resistance. If there is any *local* fracture in carbon fiber, the value of contact resistance might not change significantly, as the asperity contact would be in touch with the fiber surface walls.

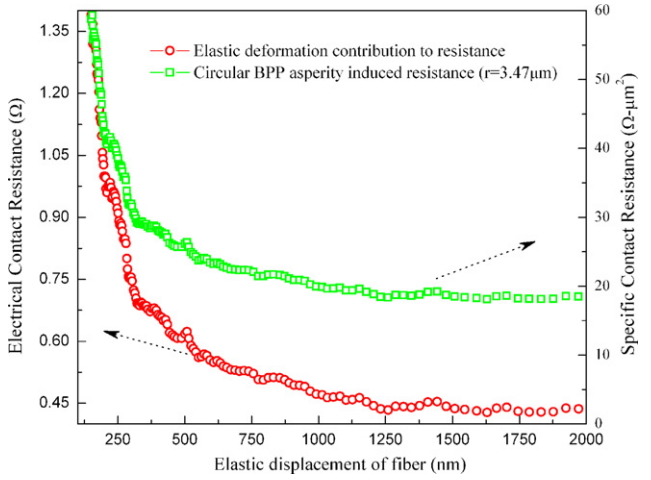

Fig. 8. Electrical contact resistance variation over carbon fiber elastic deformation.

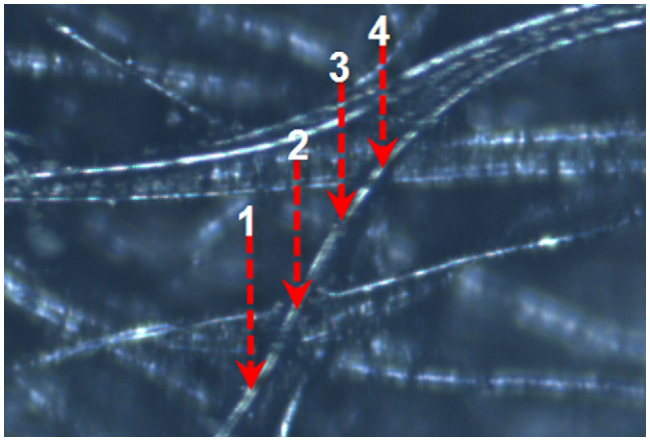

Fig. 9. Randomly distributed carbon fibers on GDL and arrows indicate the indentation points.

4.3. Fracture toughness of Teflon® coated carbon fiber

Mechanical properties may vary from one carbon fiber to another or one place to another and so is the fracture toughness measurement. In order to avoid incorrect conclusion on fracture related failure, as many as 20 indentation tests were performed with each four on one carbon fiber, chosen randomly. Fig. 9 shows the carbon fibers distributed on GDL surface taken from built-in optical microscope attached to the nanoindentation-testing machine. Thus, it was possible to select the indentation points on individual carbon fibers to estimate their mechanical properties and hence the fracture toughness.

Based on analytical approach described in Section 2, failure stress–strain is initially calculated from experimentally obtained load–displacement indentation curves. Hence, it is possible to obtain the probability distribution of failure of carbon fiber with respect to its fracture strength. Only 16 tests were successful in obtaining the fracture points, rest of them did not show any fracture like characteristics ('pop-in'). Fig. 10 shows the plot of failure stresses and failure probability distribution of carbon fiber. Fracture toughness (flexural strength) of Teflon® coated carbon fiber is found to fall in the range of 150–380 MPa. However, majority of them (nearly 10 test results) fall in 225–270 MPa range where the probability of failure is in the range of 55–88%. Hence, fracture toughness of Teflon® coated carbon fiber can be averaged to 250 MPa.

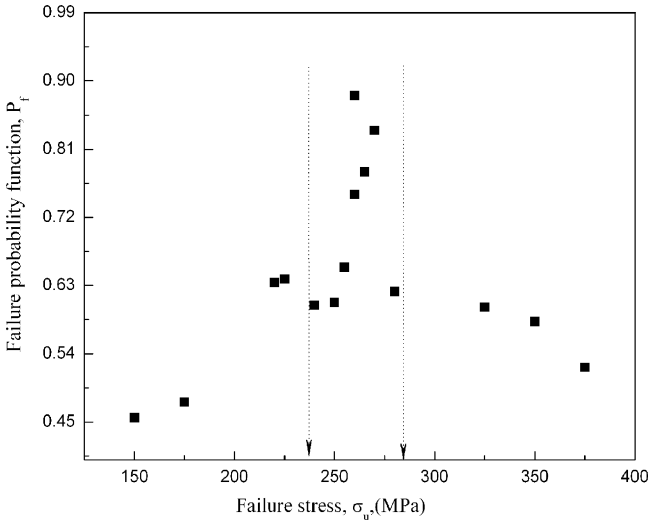

Fig. 10. Fracture toughness distribution of carbon fiber plotted in terms of probability of failure.

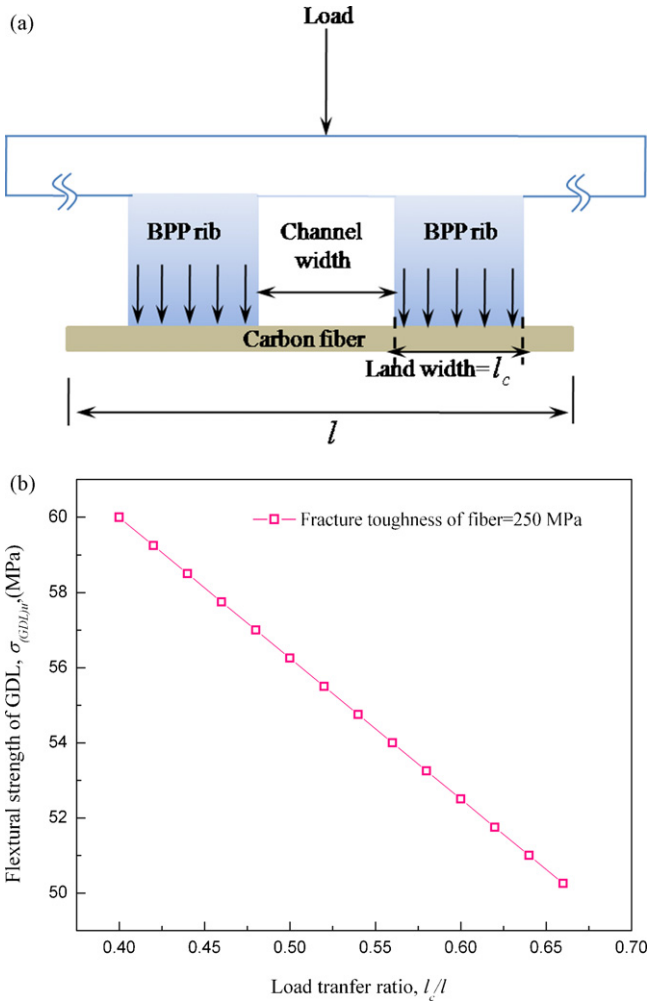

Fig. 11. (a) Schematic representation of interaction between BPP land area and carbon fiber. Land width is made equal to the load transferring length to account for the fracture toughness variations. (b) Plot of flexural strength of GDL over load transfer ratio.

4.4. Structural failure of GDL

Mechanical failure of GDL originates when the fibers are no longer capable of bearing a load exceeding its fracture limit. However, it is illogical to comment on the structural integrity of GDL based on the fracture of one carbon fiber. But the fact is when fracture occurs in one carbon fiber, load bearing capacity is transferred to adjacent matrix or fiber. (It is noted that the volume fraction of matrix in GDL is very less and load is assumed to transfer completely to fiber.) Hence, fracture in GDL is continuous and not an instantaneous process. Based on analytical calculations, ratio of load transfer length to fiber length in fuel cell is found to vary from 0.4 to 0.66. This is achieved by taking the BPP land area as a load transfer length (for each BPP contact on carbon fiber load transfer length is equal to the BPP land width) and fiber length is made as a variable length as shown in Fig. 11(a). As the fiber length increases, load transfer length also changes, according to which limits for the lengths can be found easily. Linear variation of flexural strength of GDL based on ultimate strength of carbon fiber, volume fraction of fiber (30%), and load transfer length is shown in Fig. 11(b). The values vary from 60 to 50 MPa.

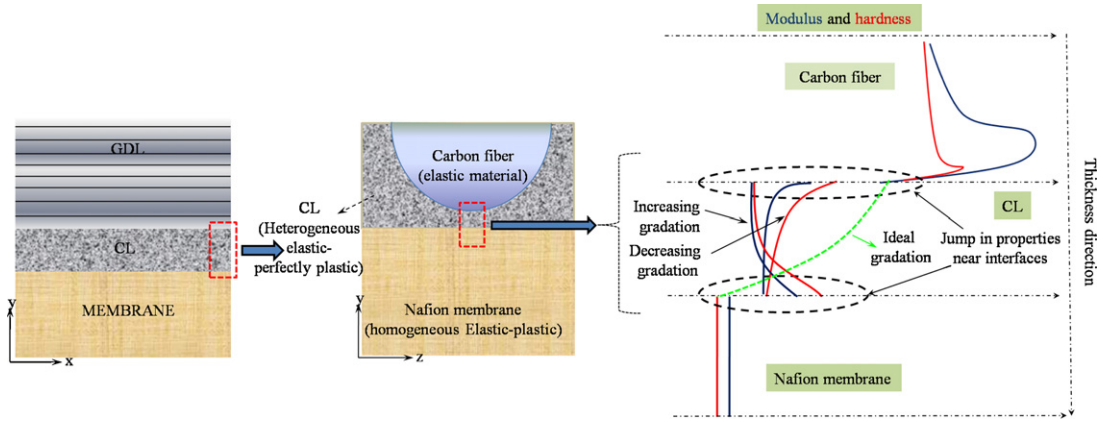

Fig. 12. Structural integrity principle. (a) Membrane electrode layers, (b) interaction of CL, carbon fiber and membrane near interfaces. (c) Mechanical property variations indicating the property jumps near interfaces (d) ideal property variation to favor the smooth force transition and damage resistance.

4.5. Structural integrity principle of MEA

State-of-the-art structural integrity principle of MEA near interfaces is unlocked after successfully obtaining the mechanical properties of CL [26] and carbon fiber at nano-level. Fig. 12 shows the modulus and hardness variation along the thickness direction near the interface. Focusing mainly on the interface region between GDL/CL and GDL/membrane, abrupt changes in properties in the interface is believed to be one of the reasons for interfacial failure. As shown in Fig. 12 interface stress transition is better understood by scaling the interfaces to micro-level. This is particularly important as damage or fracture at microscopic level affects the material strength of the macroscopic mechanical response. Further, carbon fiber of GDL is a brittle material and possesses to have a high strength as compared to ductile CL. There is a jump in material properties near GDL/CL interface, making the interface inappropriate for a smooth stress transition. This invites a driving force for the delaminations as well as cracks in CL surface. Let us consider an increasing gradation of mechanical properties in CL [26] and now this is a subject of interest for crack propagation from the surface to the bottom of the CL. Qualitative analysis of driving force for the crack propagation in an increasing gradation direction is reported in Section 4.6. Irrespective of crack that may or may not be arrested, interfacial zone between CL and membrane becomes rather significant in damage evolution in CL. As can be seen from Fig. 12 there is an abrupt change in properties from CL to membrane. Hence, it is expected that inelastic strain accumulation in the membrane near interface would be large (justified in [26]) and its subsequent effect on damage accumulation may cause an interface delamination upon many loading cycles. On the other hand, there is a high possibility of catalyst cracking (ductile fracture) near the interface because of local stress concentration resulted from abrupt stress transition.

An ideal way of stress transition from GDL to membrane is shown in Fig. 12. However, it may or may not be able to achieve this target as it may affect overall electro-chemical performance of the cell which is very important. Further, present analysis does not involve any of interfacial chemical interactions, which is also very important in acceleration or propagation or evolution of damage. Even if the hygrothermal effect (HTE) is taken into consideration, overall structural integrity 'principle' of the fuel cell layer may not have altered in a big way, as HTE is believed to accelerate an existing damage. For example, total energy required for the interfacial separation between CL and membrane can be related to the energy release rate associated with the crack extension. For elastic–plastic materials like CL and membrane, energy release rate is given by the following equation:

$$\Gamma = 2\gamma_s + \gamma_p \tag{32}$$

where γ_s is the free energy of the newly created surface upon crack extension and γ_p is the energy dissipated through irreversible processes (chemical or mechanical).

Introduce a thermal environment and consider each layer having a different thermal expansion coefficient. Now the thermal strain mismatch (ε_r) in the CL with respect to membrane is given by

$$\varepsilon_r = (\alpha_m - \alpha_{cl})\Delta T \tag{33}$$

where α_m and α_{cl} are the coefficient of thermal expansion of membrane and CL, respectively.

Given the catalyst layer thickness, t, thermal strain can be used in finding the energy contribution for interfacial separation without any external applied loading and is given by the following equation [40]:

$$\gamma_t = \frac{t}{2}\frac{(1+\upsilon_{cl})E\varepsilon_r^2}{(1-\upsilon_{cl})} \tag{34}$$

where υ_{cl} is the Poisson's ratio of CL. E represents its modulus.

Now the energy release rate can be rewritten according to the following equation:

$$G = 2\gamma_s + (\gamma_p - \gamma_t) \tag{35}$$

According to Eq. (35), energy release rate to propagate a crack is decreased by an amount of γ_t, i.e., delamination process is accelerated. It is also true when humidity related strain is considered.

4.6. Driving force for crack propagation

Driving force for the crack propagation in CL is investigated based on the gradation in the mechanical properties. Here the stress intensities near the crack tip become important in predicting the crack propagation. Fig. 13(a) shows the contour plot of stress intensities of three-layer model with a pre-existing crack. High stress intensities can be found near the lower crack tip and it is observed to extend ahead for some distance. This is due to the higher amount of energy release rate in CL where the properties are decreasing. In contrast to this result, stress intensities are much less near the upper crack tip due to lesser energy release rate where the properties are increasing. Hence, it can be concluded that crack can easily propagate in case of decreasing gradation whereas it may mitigate in case of increasing gradation. Further, referring to Fig. 13(b), large difference can be pointed out in terms of stress distribution

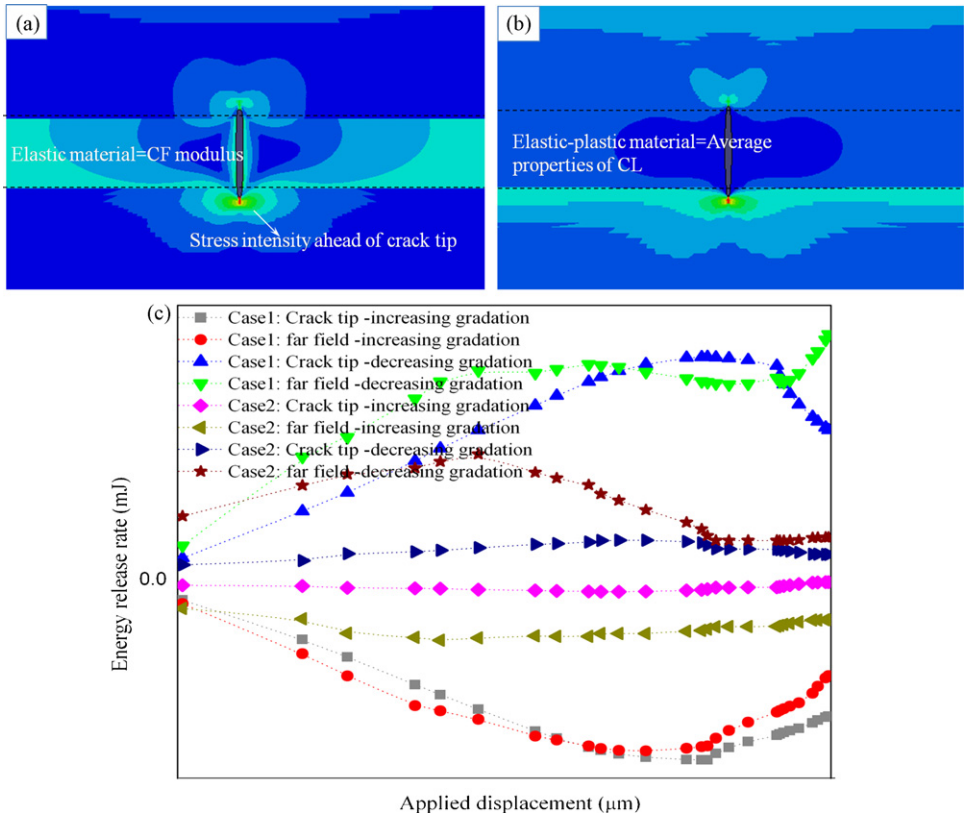

Fig. 13. Driving force for crack propagation. (a) Case 1: contour plot of stress intensities near crack tips under hard interlayer. (b) Case 2: effect of elastic–plastic interlayer on the stress intensity distribution near crack tips. (c) Qualitative plot of energy release rate in both of crack tips under two different cases.

as opposed to Fig. 13(a). The stress intensity near the lower crack tip in Fig. 13(b) is observed to be less than in case of Fig. 13(a). This suggests that crack propagation can also be influenced by the adjacent layer properties as well. In the first case, middle layer is taken to be a hard elastic material whose properties are equated to carbon fiber modulus, representing an exact scenario of GDL/CL interface interaction. In the second case, middle layer is replaced with the elastic–plastic material with the average CL properties (modulus = 450 MPa; Yield strength = 65 MPa) to typify the difference of adjacent layer material properties on crack propagation.

In order to understand the effect of gradations and the medium from which crack propagates, energy release rate is plotted for all the cases, which includes crack tip J-integral and far field J-integral and is shown in Fig. 13(c). In general, it can be observed that, for all increasing gradation cases energy release rate is negative below the zero-limit indicating the crack mitigation. In addition, for all decreasing gradation cases, energy release rate is above zero-limit indicating the crack propagation. Under Case 1, for the decreasing gradation CL, far field integral appears to increase further whereas crack tip integral appears to mitigate. This observation is very significant as the increasing far field crack intensity represents a growing damage into the surface. In contrast to this result, far field integral under Case 2, for the decreasing gradation in CL, decreases to a near-negative value indicating a crack arrest. Two contradicting results under the same gradation conditions in CL are now said to have been affected by a medium (interlayer) from which crack propagates.

This is a qualitative analysis to investigate the probabilities of crack propagation under different circumstances but is related to the fuel cell damage mechanics. Hence, in general two things can be concluded here. Firstly, crack propagation in the increasing gradation of properties in CL mitigates whereas in a decreasing gradation it intensifies. Secondly, layer properties from which crack initiates are also an influencing factor for the crack propagation. Hard layer (correspond to carbon fiber of GDL) from which crack initiates (and grows to an adjacent decreasing gradation of CL) is found to magnify the crack propagation whereas soft or relatively weaker layer from which crack initiates is found to mitigate the crack propagation in decreasing gradation of CL.

4.7. Crack propagation in cell layers (mechanical perspective)

Fig. 14 shows the variations in reaction force with respect to the separation displacement under three cases of CL property vari-

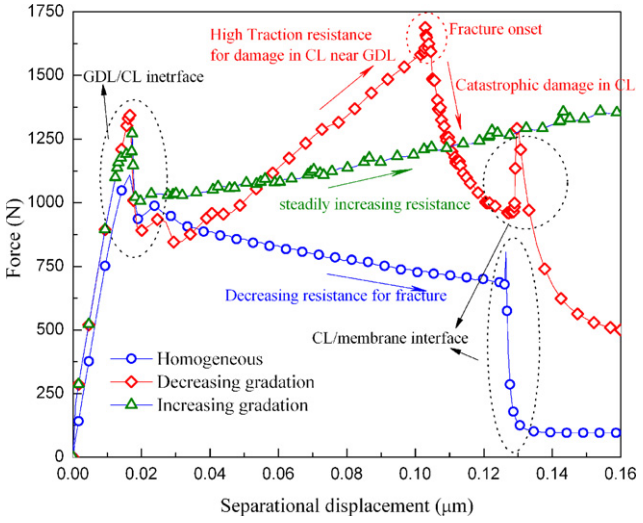

Fig. 14. Reaction force vs. separation displacement for the cohesive zone model described in Fig. 3 under three different cases of property variations in CL.

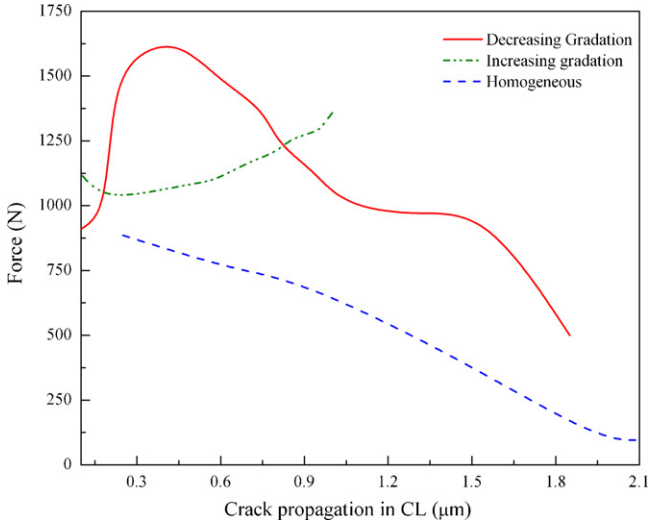

Fig. 15. Crack propagation length in CL under three property conditions.

ations. Curves explain the significance of material gradation in understanding the crack propagation in CL and related failures. Plot can be broadly classified into two interfacial zones, namely, GDL (carbon fiber)/CL interface and CL/membrane interface. Initial peak shows the onset of fracture in GDL/CL interface, representing a maximum traction-displacement resistance, beyond which element fails and delamination or crack propagates to CL. From this point onwards, crack propagation entirely depends upon the magnitude of traction resistance posed by the cohesive elements. For homogeneous CL (averaged CL properties), fracture resistance decreases as the damage proceeds without any obstruction. When it reaches to CL/membrane interface, there is a sudden jump (decrease) in the resistance force and this corresponds to a weaker interface. Cohesive element properties of membrane zone are scaled according to its elastic-plastic properties. Hence, any influence of creep or viscoplastic effect of membrane on the fracture behavior is neglected at this stage.

Further, as expected for the increasing gradation of CL, fracture resistance (toughness) for the damage increases and thus the separation displacement as well as the maximum force required is obviously large. After the initial interfacial breakage (GDL/CL), quantification of fracture toughness near CL/membrane interface becomes very difficult from the present plot (Fig. 14) alone. Hence, crack propagation length in CL is plotted against the reaction force as shown in Fig. 15. For every 10 increments of step-time, the results are monitored. As can be seen from the Fig. 15, crack propagation in homogeneous CL material is a linear function of decreasing force. On the other hand, for inhomogeneous-increasingly graded (from GDL side) CL, force required is substantially high and crack mitigates after being propagated for nearly 0.9 μm.

Interestingly, for the decreasing gradation of CL, initial fracture energy required to break the cohesive bond is very high and once the maximum limit reaches, there is a catastrophic failure in the CL as can be observed from Fig. 14. After the sudden fall in force, damage propagates to the CL/membrane interface. Fracture resistance of CL/membrane in this case marginally increases from its homogeneous counterpart due to the inhomogeneity induced in CL. Again, Fig. 15 can be referred to estimate the crack propagation length in CL under decreasing gradation. In order to propagate initial crack length of 300 nm, force required is higher than any other cases. However, once the damage initiates it propagates catastrophically. It is worth noting that the separation displacement of 0.1–0.13 μm in Fig. 14 (decreasing gradation) is equal to crack length propagation from 0.35 to 1.9 μm in Fig. 15.

Above cohesive zone model is a micro-mechanical model based on the principles of continuum mechanics. Hence, the quantification of above results may not hold reasonable when the problem is perceived in the atomistic level (this specifically refers to the maximum traction and separation displacement values and definitely not the mode of crack propagation). Qualitative analysis of damage propagation in cell layers and interfaces presented in this paper should be sufficient to understand the influence of material inhomogeneities.

5. Concluding remarks

As the researches on innovative materials for fuel cell is advancing with a rapid pace, it is always necessary to lay a foundation based on structural integrity. Factors affecting the structural integrity of GDE are investigated in this paper. Fuel cell layers are prone to chemical, mechanical, and thermal degradation. This paper gives an insight into the mechanical related failures and their propagation in GDE and we believe this will provide necessary information regarding the long-standing debate on mechanical durability. Studying the mechanical properties at a smaller scale (micro/nano-scale) is the key to acquire basic information regarding the failure of layers.

Flexural strength of GDL is investigated after experimentally determining the mechanical properties of carbon fiber. Inhomogeneity in properties is recorded in terms of hardness, modulus, and contact stiffness. Influence of these properties on electrical contact resistance and flexural strength of carbon fiber as well as GDL are investigated by introducing the moderate changes to the fundamental relations. Ductile (elastic–plastic loading event during the indentation experiment) to brittle transition (elastic loading with a 'pop-in' event) is observed within the carbon fiber. This nature of the material response explains the causes for surface rupture, hydrophobic coating deterioration, and breakage of the fiber under fuel cell loading and working conditions.

Assuming CL as an interlayer between membrane and GDL, damage propagation has been investigated on a much broader sense. Since not many literatures are available on mechanical principles of CL, studies presented in this article dealing with the damage or crack propagation based on inhomogeneities of CL are very useful in understanding the surface crack (near GDL/CL) or interface crack (initiated from the damage accumulation in membrane or CL itself (local fracture due to stress concentrations at critical locations [26])) evolutions. Overall structural integrity principle is explained and the technical problems associated with those are addressed clearly.

Acknowledgements

This research was supported by Inha University. Authors are thankful to 'Inha Collaborative Research Instruments' for providing the necessary information in using the experimental devices.

References

[1] K.H. Lim, H.S. Oh, S.E. Jang, Y.J. Ko, H.J. Kimb, H. Kim, Journal of Power Sources 193 (2009) 575–579.
[2] N.Y. Steinera, Ph. Mocotéguy, D. Candussoc, D. Hissel, Journal of Power Sources 194 (2009) 130–145.
[3] S. Zhang, X. Yuan, H. Wang, W. Mérida, H. Zhu, J. Shen, S. Wu, J. Zhang, International Journal of Hydrogen Energy 34 (2009) 388–404.
[4] J. Wu, X.Z. Yuan, J.J. Martin, H. Wang, J. Zhang, J. Shen, S. Wu, W. Merida, Journal of Power Sources 184 (2008) 104–119.
[5] F.A. de Bruijn, V.A.T. Dam, G.J.M. Janssen, Fuel Cells 08 (2008) 3–22.
[6] S. Zhang, X.Z. Yuan, J.N.C. Hin, H. Wang, K.A. Friedrich, M. Schulze, Journal of Power Sources 194 (2009) 588–600.
[7] Y. Hiramitsu, H. Sato, H. Hosomi, Y. Aoki, T. Harada, Y. Sakiyama, Y. Nakagawab, K. Kobayashi, M. Hori, Journal of Power Sources 195 (2010) 435–444.

[8] M. Marrony, R. Barrera, S. Quenet, S. Ginocchio, L. Montelatici, A. Aslanides, Journal of Power Sources 182 (2008) 469–475.
[9] W. Schmittinger, A. Vahidi, Journal of Power Sources 180 (2008) 1–14.
[10] Z.B. Wang, P.J. Zuo, Y.Y. Chu, Y.Y. Shao, G.P. Yin, International Journal of Hydrogen Energy 34 (2009) 4387–4394.
[11] L. Cindrella, A.M. Kannan, J.F. Lin, K. Saminathan, Y. Ho, C.W. Lin, J. Wertz, Journal of Power Sources 194 (2009) 146–160.
[12] L.R. Jordan, A.K. Shukla, T. Behrsing, N.R. Avery, B.C. Muddle, M. Forsyth, Journal of Applied Electrochemistry 30 (2000) 641–646.
[13] S.G. Kandlikar, Z. Lu, T.Y. Lin, D. Cooke, M. Daino, Journal of Power Sources 194 (2009) 328–337.
[14] I. Nitta, T. Hottinen, O. Himanen, M. Mikkola, Journal of Power Sources 171 (2007) 26–36.
[15] I. Nitta, O. Himanen, M. Mikkola, Fuel Cells 8 (2008) 111–119.
[16] J.H. Lin, W.H. Chen, Y.J. Su, T.H. Ko, Fuel 87 (2008) 2420–2424.
[17] A. Bazylak, D. Sinton, Z.-S. Liu, N. Djilali, Journal of Power Sources 163 (2007) 784–792.
[18] Z. Wu, S. Wang, L. Zhang, S.J. Hub, Journal of Power Sources 189 (2009) 1066–1073.
[19] J. Kleemann, F. Finsterwalder, W. Tillmetz, Journal of Power Sources 190 (2009) 92–102.
[20] B. Avasarala, P. Haldar, Journal of Power Sources 188 (2009) 225–229.
[21] C.J. Bapat, S.T. Thynell, Journal of Power Sources 185 (2008) 428–432.
[22] Z. Wu, Y. Zhou, G. Lin, S. Wang, S.J. Hu, Journal of Power Sources 182 (2008) 265–269.
[23] X. Lai, D. Liu, L. Peng, Ni Jun, Journal of Power Sources 182 (2008) 153–159.
[24] Y. Zhou, G. Lin, A.J. Shih, S.J. Hu, Journal of Power Sources 163 (2007) 777–783.
[25] M. Mathias, J. Roth, J. Fleming, W. Lehnert, Handbook of Fuel Cells—Fundamentals, Technology and Applications, vol. 3, John Wiley and Sons, 2003.
[26] K.K. Poornesh, C.D. Cho, G.B. Lee, Y.S. Tak, "Gradation of mechanical properties in Gas Diffusion Electrode – Part 1: Influence of nano-scale heterogeneity in Catalyst Layer on interfacial strength between Catalyst Layer and membrane", Journal of Power Sources, in press.
[27] J.R. Barber, Proceedings of the Royal Society of London A 459 (2003) 53–66.
[28] Zhiqiang Cao, Xin Zhang, Thin Solid Films 516 (2008) 1941–1951.
[29] B.D. Agarwal, L.J. Boutman, Analysis and Performance of Fiber Composites, John Wiley & Sons, New York, 1980.
[30] D. Hull, An Introduction to Composite Materials, Cambridge University Press, 1981.
[31] O. Kolednik, International Journal of Solids and Structures 37 (2000) 781–808.
[32] Y. Sugimura, P.G. Lim, C.F. Shih, S. Suresh, Acta Metallica Materiala 43 (1995) 1157–1169.
[33] A.S. Kim, S. Suresh, International Journal of Solids and Structures 34 (1997) 3415–3432.
[34] F. Rong, C. Huang, Z.S. Liu, D. Song, Q. Wang, Journal of Power Sources 175 (2008) 699–711.
[35] F. Rong, C. Huang, Z.S. Liu, D. Song, Q. Wang, Journal of Power Sources 175 (2008) 712–723.
[36] L.Y. Jiang, Y. Huang, H. Jiang, G. Ravichandran, H. Gao, K.C. Hwang, B. Liu, Journal of the Mechanics and Physics of Solids 54 (2006) 2436–2452.
[37] W.B. Lu, J. Wu, J. Song, K.C. Hwang, L.Y. Jiang, Y. Huang, Computer Methods in Applied Mechanics and Engineering 197 (2008) 3261–3267.
[38] ABAQUS Analysis User's Manual, Hibbitt, Karlsson & Sorensen, Inc., 2007.
[39] A. Kusoglu, A.M. Karlsson, M.H. Santare, S. Cleghorn, W.B. Johnson, Journal of Power Sources 161 (2) (2006) 987–996.
[40] L.B. Freund, S. Suresh, Thin Film Material: Stress, Defect Formation and Surface Evolution, Cambridge University Press, 2003.